Retrieving tropospheric NO₂ vertical column densities around the city of Beijing and estimating NOX emissions based on Car MAX-DOAS measurements

Xinghong Cheng[1], Jianzhong Ma[1], Junli Jin[2], Junrang Guo[1], Yuelin Liu[2], Jida Peng[4], Xiaodan Ma[5], Minglong Qian[6], Qiang Xia[6], Peng Yan[2]

[1]State Key Lab of Severe Weather & Key Laboratory for Atmospheric Chemistry, Chinese Academy of Meteorological Sciences, Beijing 100081, China

[2]CMA Meteorological Observation Centre, Beijing 100081, China

[3]College of Electronic Engineering, Chengdu University of Information Technology, Chengdu 610225, China

[4]Meteorological Institute of Fujian, Fuzhou 350001, China

[5]Nanjing University of Information Science and Technology, Nanjing 210044, China

[6]China National Huayun Technology Development Corporation, Beijing 100081, China

Correspondence to: Xinghong Cheng (cxingh@cma.gov.cn) and Jianzhong Ma (majz@cma.gov.cn)

Abstract. We carried out 19 city-circle-around Car MAX-DOAS experiments on the 6th Ring Road of Beijing in January, September, and October 2014. The tropospheric vertical column densities (VCDs) of NO₂ were retrieved from measured spectra by the Multi-Axis Differential Optical Absorption Spectroscopy (MAX-DOAS) technique and used to estimate the emissions of NO$_x$ ($\equiv$ NO + NO₂) from urban Beijing during the experimental periods. The offline LAPS-WRF-CMAQ model system was used to simulate the wind fields by assimilation of observational data and calculate the NO₂-to-NO$_x$ concentration ratios, both of which are also needed for the estimation of NO$_x$ emissions. The NO$_X$ emissions in urban Beijing for the different months derived from the Car MAX-DOAS measurements in this study were compared to the multi-resolution emission inventory in China for 2012 (MEIC 2012). Our Car MAX-DOAS measurement results showed higher NO₂ VCD in January than in the other two months. The wind field had obvious impacts on the spatial distribution of NO₂ VCD, with the mean NO₂ VCD along the 6th Ring Road typically being higher under the south wind than under the north wind. In addition to the seasonal difference, the journey-to-journey variations of estimated NO$_X$ emissions rates (E$_{NOX}$) were large even within the same month, mainly due to uncertainties in the calculations of wind speed, the ratio of NO₂ and NO$_X$ concentration, and the decay rate of NO$_X$ from the emission sources to the measured positions under different meteorological conditions. The ranges of E$_{NOX}$ during the heating and non-heating periods were 22.59×10^{25} to 31.28×10^{25} molecules s^{-1} and 9.61×10^{25} to 11.96×10^{25}

molecules s^{-1}, respectively. The average E$_{NOX}$ values in the heating and non-heating periods were 26.94 $\pm$ 6.14 $\times$ 10^{25} molecules s^{-1} and 10.99 $\pm$ 1.23 $\times$ 10^{25} molecules s^{-1},, respectively. The uncertainty range of E$_{NOX}$ was 19.52–52.01%. The monthly emission rates from MEIC 2012 are found to be lower than the

35   estimated E$_{NOX}$, particularly in January. Our results provide important information and datasets for the validation of satellite products and also show how Car MAX-DOAS measurements can be used effectively for dynamic monitoring and updating of the NO$_x$ emissions from megacities such as Beijing.

1.   Introduction

40   Over the past decade, serious haze events have occurred frequently in autumn and winter in Beijing due to massive anthropogenic emissions from the combustion of fossil fuels and other sources (He et al., 2013; Zhang et al., 2013). High concentrations of aerosol particulate matter with dynamic diameter less than 2.5 μm (PM$_{2.5}$) threaten public health (Cao et al., 2014), disturb traffic operation by affecting visibility, and result in perturbations to the weather and climate by scattering

45   and absorption of solar radiation (Liao et al., 2015; Cheng et al., 2017). Measurements have shown that organic matter (OM), sulfate, nitrate, and ammonium made up more than 78% of the PM$_{2.5}$ in January 2013 in Beijing (Huang et al., 2014). Fractions of nitrate in PM$_{2.5}$ have increased recently with the control of industry and coal in the Beijing-Tianjin-Hebei region, which has reduced SO$_2$ emissions and the ratio of sulfate in PM$_{2.5}$, while traffic emissions are still at high levels. A recent study based on the aerosol

50   observations at the campus of Peking University in 2014 revealed that aerosol pollution is nitrate-driven in spring and early fall and OM-driven in late fall and winter (Tan et al., 2018). The study suggested that nitrate formation was more significant than sulfate formation during severe pollution episodes in Beijing. Therefore, studies on the spatiotemporal variation of NO and NO$_2$ (together denoted as NO$_X$), with the latter being a precursor of nitrate aerosols, are very important for understanding the aerosol formation

55   and its influencing factors.

Emission inventories are usually developed by the so-called bottom-up approach, which is based on combinations of activity statistics (such as energy consumption and industrial production) and source- or region-specific emission factors (Hao et al., 2002; Zhang et al., 2007; Zhao et al., 2012; Streets et al., 2013). However, there are large uncertainties in bottom-up emissions inventories associated with the

60   statistics, emissions factors, temporal allocation profiles, and grid allocation factors (Ma and Van Aardenne, 2004; Zhao et al., 2012). Moreover, estimating "current" emissions by the bottom-up

methodology is fundamentally difficult because publication of basic statistics is generally a couple of years behind. The "top-down" emission estimate is a useful supplement to bottom-up estimates, which are subject to uncertainties in emissions factors and emissions activities (Streets et al., 2013). Inverse modeling, in which emissions are optimized to reduce the differences between simulated and observed data, is a powerful method that solves the problems of the bottom-up approach. Recently, its application to the estimation of NO_X emissions has been widely reported. NO_X emission rates are derived by constraining satellite observations using the relationship between model-simulated NO_2 vertical column density (VCD) and primary NO_X emission estimates from the bottom-up approach (Martin, 2002; Jaegle' et al., 2005; Konovalov et al., 2006; Wang et al., 2007; Lin et al., 2012; Zyrichidou et al., 2015). Nevertheless, errors and uncertainties still exist in the retrieval of satellite data, which leads to a large decrease in the accuracy of estimated emissions, particularly in highly polluted regions such as Beijing and its surroundings (Ma et al., 2013a; Jin et al., 2016). Uncertainties can arise from noise, surface albedo, cloud blocks, profile shape, interference from ozone absorption, correlations with other retrieved parameters, fitting wavelength window, and so forth (Jin et al., 2016; Ma et al., 2013a; Shaiganfar et al., 2011, 2017). Air mass factor (AMF) errors can produce additional errors during the conversion process from the slant to vertical columns. Therefore, comprehensive ground-based measurements of the tropospheric columns and vertical profiles of NO_2 are quite important and necessary to evaluate and validate satellite retrieval products.

The Multi-Axis Differential Optical Absorption Spectroscopy (MAX-DOAS) is a ground-based remote sensing technique developed during the last two decades. It makes use of the scattered sunlight measured from horizontal through zenith pointing direction to retrieve the VCD and vertical profiles of trace gases and aerosols with relatively high sensitivity in the lower atmosphere (Hönninger et al., 2004; Wagner et al., 2004; Platt and Stutz, 2008). MAX-DOAS has been extensively used to derive tropospheric column information of NO_2 and some other pollutants in various regions(Wittrock et al., 2004; Brinksma, et al., 2008; Irie et al., 2008; Vlemmix et al., 2010; Li et al., 2013; Hendrick et al., 2014; Tan et al., 2008; Wagner et al.,2011). Mobile- (or Car-) MAX-DOAS measurements have been used to quantify NO_X emissions from cities and regions such as Beijing (Johansson et al., 2008), Mexico (Johansson et al., 2009), Mannheim and Ludwigshafen (Ibrahim et al., 2010), Deli (Shaiganfar et al., 2011), Shanghai (Wang et al., 2012), North China (Wu et al., 2018). Compared to ground-based observations at a fixed site, Car-MAX-DOAS measurements can provide information on the horizontal spatial distribution of

pollutants, which is important for explaining the urban/regional representativeness of satellite observations and validating the NO₂ VCDs and NOx emission estimates from the new, high pixel resolution measurements by the TROPOMI instrument on the Sentinel-5P over megacities such as Beijing. Moreover, due to the rapid expansion of urban area and increasing energy consumption, both locations and strength of emission sources in Beijing might have changed significantly. Therefore, intensive Car-MAX-DOAS measurement campaigns are still needed to estimate the emissions of NO_X in Beijing. Mean wind speed and wind direction along the ring road during the sampling periods were usually used to estimate NO_X emissions in previous studies. Since wind field changes rapidly due to local circulation and then results in uncertainties in quantification of NO_X emissions (Johansson et al., 2008; Shaiganfar et al., 2011, 2017; Davis, et al., 2019), refined and accurate simulations of wind fields are needed for the accurate emission estimate.

In this study, we estimated the total NO_X emissions from urban Beijing based on the VCD of NO₂ obtained from intensive Car MAX-DOAS measurements on the 6th Ring Road of Beijing in January, September, and October of 2014. The offline LAPS-WRF-CMAQ model system with data assimilation method was used to derive wind speed, wind direction, and NO₂/NO_X concentration ratios, which are needed to estimate total urban NO_X emissions based on Car MAX-DOAS measurements. We attempted to accurately estimate the NO_X emission rates and the seasonal difference and deeply investigate the uncertainties and appropriate meteorological conditions for the estimation based on Car MAX-DOAS measurements. This paper is organized as follows: Section 2 describes the intensive Car MAX-DOAS experiments and the retrieval method for deriving tropospheric NO₂ VCD, the model system used to simulate the wind fields and the ratios of NO₂ and NO_X, and the method used to quantify total NO_X emissions. Section 3 presents the results of the NO₂ VCD and the estimated NO_X emissions as well as their uncertainties due to simulated errors in the wind field. Conclusions are provided in Section 4.

2. Theory, experimental, and method

2.1 Formula to estimate urban NOx emissions

The complete NO₂ flux F_{NO_2} across the urban Beijing area encircled by the driving route S is estimated according to the closed integral method (CIM)of Ibrahim et al. (2010).

$$F_{NO_2} = \oint_s VCD_{NO_2}(s) \cdot \vec{w} \cdot \vec{n} \cdot ds \tag{1}$$

Here $VCD_{NO_2}(s)$ is the NO₂ VCD at the sampling position within the driving route; $\vec{n}$ indicates the normal vector parallel to the Earth's surface and orthogonal to the driving direction at the position of the driving route; $\vec{w}$ is the average wind vector within the NO₂ layer, which is denoted by wind speed at the height of 10 m. We carried out Car MAX-DOAS measurements along closed driving routes around large emissions sources, i.e., the 6th Ring Road of Beijing (Fig. 1).

We averaged the wind vector data from the WRF model between surface and 1000m altitude weighted by the winter exponentially decreasing profiles according to the method of Shaiganfar et al. (2017).

$$\vec{w} = \frac{\sum_i w(z_i).e^{-\frac{z_i}{z_0}}}{\sum_i e^{-\frac{z_i}{z_0}}} \tag{2}$$

Hear $w(z_i)$ is the wind vector at altitude z_i, and z_0 indicates the assumed scale height of 300m for winter.

According to the CIM, the complete NO_X emissions from the encircled areas are determined considering the partitioning between NO and NO₂ (c_L) and the finite lifetime of NO_X (c_τ).

$$E_{NO_x} = c_L \cdot c_\tau \cdot F_{NO_2} \tag{3}$$

$$c_L = \frac{c_{NO_x}}{c_{NO_2}} \tag{4}$$

Here c_L is simply the ratio of NO_X (C_{NO_x}) and NO₂ (C_{NO_2}) bulk concentration in the polluted layer which are simulated by the CMAQ model in this study. It is a function of the Leighton ratio (Lc=[NO]/[NO₂]), c_L=1+Lc. To analyze whether there is or not the impact of VOCs on lifetime of NO_X, we also calculate another Leighton ratios, L_r, referring to the method of Davis et al. (2019).

$$L_r = \frac{j_{NO_2}[NO_2]}{k_8[NO][O_3]} \tag{5}$$

Where j_{NO_2} is the NO₂ photolysis rate, k_8 is the temperature-dependent rate constant for the reaction between NO and O₃. We calculate j_{NO_2} according to the method of Dickerson et al., 1982

c_τ describes the decay of NO_X from the emission sources to measured positions. c_τ can be estimated from the NO_X lifetime τ, which is the reciprocal of the product of reaction rate constant k, OH concentration (C_{OH}) and air density (M)(Ma et al., 2013), and transport time t, which is the distance between emission source and sampling point r divided by the wind speed $\vec{w}$.

$$c_\tau = e^{\frac{t}{\tau}} = e^{\frac{r/\vec{w}}{\tau}} \tag{6}$$

$$\tau = \frac{1}{k*C_{OH}*M} \tag{7}$$

We firstly calculated averaged simulated wind speed and direction, the ratio of NO_X and NO_2, and the NO_x lifetime from surface to 1000m at every sampling position on the 6th Ring Rd of Beijing for each journey, and computed the distance between the sampling position and the center of the city of Beijing for r. Then, we computed the c_τ, F_{NO2}, and E_{NOX}. The lifetime τ was calculated with simulated average OH concentration and air density from surface to 1000m at each sampling position for each journey.

2.2 Car MAX-DOAS measurements

2.2.1 Instrument and experiment

We measured and retrieved tropospheric NO_2 VCD along the sixth ring road of Beijing (hereafter referred to as 6th Ring Rd) in January, September, and October of 2014 using a Mini MAX-DOAS instrument mounted on the vehicle.

The instrument, manufactured at Hoffmann Messtechnik GmbH, Germany, is a fully automated, light-weighted spectrometer designed for the spectral analysis of scattered sunlight by the MAX-DOAS technique (Hönninger et al., 2004; Davis et al.,2019). The same type of instrument was used in previous studies, including long-term site measurements in Beijing (Ma et al., 2013a)and a Car MAX-DOAS observational journey in Europe (Wagner et al., 2010a). The instrument consists of a hermetically sealed metal box of approximately 3 liter volume containing entrance optics, fiber coupled spectrograph and all electronics. A spectrometer with the model Ocean Optics USB2000+ is used. A stepper motor, adjusted outside the box, rotates the whole instrument to control the elevation viewing angle. The spectrograph covers the range 292-436 nm and its entrance slit is 50 μm wide. A Sony ILX511 CCD (charged coupled device) detects the light in 2048 individual pixels. The whole spectrograph is cooled by a Peltier stage to guarantee a stable temperature of the optical setup and a small dark current signal. For this study, the instrument was mounted on the roof of a car. Inside the car, two 12V DC batteries alternatively supplied electronic power for the running of instruments and a laptop computer, with a script run by the DOASIS software (Kraus, 2001b) to control the measurement process and the recording of spectra. The temperature of the spectrograph was set to be maintained at –5°C in January and at 0°C in September and October, well below the ambient temperatures during the experimental days of the study. The signal spectra of dark current and electronic offset were measured each day before and after the field experiment on the road, with 10000 msec and 1 scan for dark current measurements and 3 msec and 1000 scans for

electronic offset measurements. Measurements were made alternatively at 30° and 90° elevation angles, with every 30° measurement immediately followed by a 90° measurement. Each elevation angle measurement had an integration time of about 1 min, including typically 300-400 scans for an average spectrum.

The instrument onboard the car was operated to measure scattered sunlight from the driving forward direction. There were no high buildings on both sides of the 6th Ring Rd., and the measurements were made at a wide-field view. The driving speed was typically controlled at 80–90 km h^{-1}, and it generally took about 2.0–2.5 h to complete one circle (about 187 km) around the 6th Ring Rd. Figure 1 shows the driving route of the Car MAX-DOAS experiment on a map of Beijing and spatial distribution of the yearly NO$_X$ emission rate with a resolution of 0.25° × 0.25° from the MEIC inventory in 2012, which includes transportation, power plant, residential, industry and agriculture. For this study, the field experiments were carried out on 14 selected days, with one or two circling journeys each day. In total, there are 19 circling journeys available. The sampling periods in this experiment and the meteorological conditions are listed in Table 1. The average wind speeds for experimental days in January, September, and October were 2.5, 2.5, and 2.4 m s^{-1}, the corresponding total cloud fractions were 4.9, 7.5, and 4.2, and the mean planetary boundary layer (PBL) heights were 192, 188, and 238 m, respectively. The dominant wind directions in the three months were much more variable, including north, south, , other directions, and static wind field. Since variations of wind field can affect the estimation of E$_{NOX}$, we synthetically analyze distribution of wind field using simulations from the WRF model and reanalysis data with a spatial resolution of 0.125° × 0.125° every three hours from the European Centre for Medium-Range Weather Forecasts (ECMWF). In some cases, the wind direction changed slightly within one circling journey period which is marked as south (S) or north (N) type in Table 1. However, the wind field during some journeys was convergent or divergent in some areas of Beijing which is marked as other type (O), and the wind speed was very low in three journeys which is marked as static type (St). To estimate the NOx emissions accurately using the CIM, the wind speed needs to be sufficiently high so that the transport across the encircled area is fast compared to the atmospheric lifetime of the trace gas (Ibrahim et al., 2010). In this study, we only consider the circling journeys with consistent wind field (S or N type) and relatively high wind speed to estimate the NOx emissions. The primary information for all the journeys, including 11 selected ones for emission estimation, is given in Table 1.

2.2.2 Spectral retrieval

The retrieval of NO_2 slant column densities (SCDs) is based on the DOAS method (Platt, 1994). The WinDOAS software (Fayt and Van Roozendael, 2011) was adopted to analyze the spectra in the 400-431 nm range on a daily basis. The Fraunhofer reference spectrum (FRS) was selected among the measured spectra at the 90° elevation angle each day by two steps: first, a spectrum measured around noon was chosen; second, the spectrum corresponding to the minimum NO_2 SCD derived in the preliminary analysis using the FRS from the first step was finally selected. The absorption cross sections of NO_2 at 294 K (Vandaele et al., 1998), O_3 at 221 K (Burrows et al., 1999), and the Oxygen dimer O_4 at 298 K (Greenblatt et al., 1990), as well as a FRS, a Ring spectrum calculated from the FRS by DOASIS (Kraus, 2001a) and a polynomial of third order were included in the spectral fitting process. Figure 2 shows an example of our spectral analysis for a measurement on 18 January 2014, 11:39:38 BJT. As shown in the figure, the atmospheric NO_2 absorption structure can be clearly extracted from the measured spectra.

2.2.3 Derivation of tropospheric NO₂ VCD

The trace gas VCD in the troposphere can be calculated using its SCD divided by the air mass factor (AMF) at an elevation angle, α:

$$VCD_{trop} = \frac{SCD_{trop}(\alpha)}{AMF_{trop}(\alpha)} \tag{8}$$

For the in-situ MAX-DOAS measurements, a FRS from the same elevation sequence was used in most cases, and the stratospheric absorption can be assumed to be the same during one elevation sequence. Therefore, the VCD_{trop} can be calculated by extending Eq. 8 to Eq. 9 using the so-called differential tropospheric slant column density ($DSCD_{trop}(\alpha) = SCD_{trop}(\alpha)–SCD_{trop}(90°)$) divided by the differential air mass factor ($DAMF_{trop}(\alpha) = AMF_{trop}(\alpha)–AMF_{trop}(90°)$):

$$VCD_{trop} = \frac{DSCD_{trop}(\alpha)}{DAMF_{trop}(\alpha)} = \frac{DSCD_{meas}(\alpha)}{DAMF_{trop}(\alpha)} \tag{9}$$

with $DSCD_{meas}(\alpha) = SCD_{meas}(\alpha) - SCD_{ref}$ (Wagner et al., 2010b;Ma et al., 2013a).

For the Car MAX-DOAS measurements, the trace gas concentrations can change significantly during one measurement sequence and thus the dependence of retrieved trace gas DSCDs on the elevation angle may not be so regular as for the in-situ measurements. Therefore, it would be a better choice to use a

single FRS for the analysis of all the spectra measured along the driving route (Wagner et al., 2010b).
According to Wagner et al. (2010b), Eq.9 can be further extended to

235

$$VCD_{trop} = \frac{DSCD_{meas}(\alpha) - DSCD_{offset}(SZA)}{AMF_{trop}(\alpha)}$$ (10)

where $DSCD_{offset}$ depends on the solar zenith angle (SZA) and thus local time, t_i. For each elevation
sequence i during the individual measurement day, $DSCD_{offset}$ is calculated from a single pair of
measurements with

$$DSCD_{offset}(t_i) = \frac{AMF_{trop}(90°) \cdot DSCD_{meas}(\alpha, t_i) - AMF_{trop}(\alpha) \cdot DSCD_{meas}(90°, t_i)}{AMF_{trop}(\alpha) - AMF_{trop}(90°)}$$ (11)

240   The time series of the calculated $DSCD_{offset}(t_i)$ in this study could be fitted by a low-order polynomial,
e.g., $P(x) = a_0 + a_1 \cdot x + a_2 \cdot x^2$, as a function of time. The fitted polynomial then represents the best guess
for $DSCD_{offset}$ and can be used to calculate the VCD_{trop} from Eq. 10. In this study, the AMF was calculated
by the geometric approximation (Brinksma et al., 2008; Wagner et al., 2010b), that is:

$$AMF_{trop}(\alpha) \approx \frac{1}{\sin(\alpha)}$$ (12)

245   As an illustration, Figure 3 shows the changes of individual NO_2 $DSCD_{meas}$ and $DSCD_{offset}$ for 30°
elevation angle of each sequence as a function of time on 18 January 2014. As shown in Fig. 3, a second
order polynomial fitted from individual $DSCD_{offset}$ data points as shown in Fig. 3 tends to be stable and
can be used to represent an average value of $DSCD_{offset}$.

2.3 LAPS-WRF-CMAQ model simulation

250   **2.3.1 Model setup and data**

To quantify the NO_X emissions in Beijing more accurately, refined simulations of the wind field and NO_2
to NOx concentration ratio were needed. In this study, we utilized the offline LAPS-WRF-CMAQ model
system with high spatiotemporal resolution and data assimilation technique to obtain the refined wind
speed and wind direction and an accurate ratio of NO_2 and NO_X concentration during the Car MAX-

255   DOAS experiments. The aforementioned model system includes three components: the LAPS model
(Albers et al., 1996), the WRF model (Michalakes et al., 2004), and the CMAQ model (Dennis et al.,
1996). Simulation of wind speed and direction is improved by the LAPS-WRF model, which assimilates
observed data at the surface and high layers using the one-dimensional and three-dimensional variational
assimilation method (Albers et al., 1996). The CMAQ model is used to simulate temporal-spatial

260   distribution of NO_2 and NO concentration. The Local Analysis and Prediction System (LAPS), developed

by the NOAA Earth System Research Laboratory, is used in many numerical weather forecast centers around the world. It is a mesoscale meteorological data assimilation tool that employs a suite of observations to generate a realistic, spatially distributed, time-evolving, three-dimensional representation of atmospheric features and processes (McGinley et al., 1991). The three-dimensional realistic

265   meteorological analyses field can be used as the initial condition of the WRF model and improve the simulation of wind field. WRF is a mesoscale numerical weather prediction system designed for both atmospheric research and operational forecasting needs. CMAQ is an air-quality model developed by the U.S. Environmental Protection Agency's Atmospheric Science Modeling Division. It consists of a suite of computer programs for modeling air quality issues, including reactive gases such as NO_2, NO, SO_2,

270   O_3, and others, particulate matter (PM), air toxics, acid deposition, and visibility degradation.

This study focused on Beijing at a horizontal resolution of 4 km × 4 km with 31 vertical layers of varying thickness (between the surface and 50 hPa) using a triple-nested simulation technique. The horizontal resolutions of the three sets of grids were 36 km, 12 km, and 4 km, respectively (Fig. S1a), and the output temporal interval was 1 h. The LAPS-WRF simulations were driven by FNL/NCEP

275   analysis data every 6 h during the Car MAX-DOAS experiments, with a spatial resolution of 1° × 1°. In addition, to improve the simulation of wind field and NO_2 and NO concentrations, many meteorological data of the same periods, such as wind speed, wind direction, air temperature, and relative humidity, observed at 2400 surface weather stations and by 120 radiosonde stations were assimilated into the initial field of the WRF model using the one-dimensional and three-dimensional variational assimilation

280   method in the LAPS model. The CMAQ model uses the multi-resolution emission inventory in China for the year 2012 (MEIC 2012)with 0.25° × 0.25° resolution (Zhang et al., 2009; Li et al., 2017). Hourly gridded MEIC emission datasets at a horizontal resolution of 4 km × 4 km for the CMAQ model were generated by the Sparse Matrix Operator Kernel Emissions (SMOKE) modeling system (UNC, 2014) using reasonable temporal and spatial allocation coefficients (Cheng et al., 2017). Meteorological outputs

285   from the WRF simulations were processed to create model-ready inputs for CMAQ using the Meteorology–Chemistry Interface Processor (MCIP) (Otte and Pleim, 2010). The chemical mechanism is CB05, and the boundary conditions of trace gases consist of idealized, Northern Hemispheric, mid-latitude profiles based on results from the NOAA Agronomy Lab Regional Oxidant Model. The model simulation was started one day before the first day of the experiment to avoid the spin-up problem and

290   improve the simulation accuracy.

2.3.2 Validation of simulated surface wind and NO₂

Modelled wind speeds and directions were validated by observation data from four weather stations in Beijing. Figures S2, S3 and S4 show the scatter distribution between simulated wind speed and observation, wind rose of modelled wind direction and measurements, and their time serials. We adopted the observed hourly wind speed and direction data from Nanjiao (NJ), Tongzhou (TZ), Mentougou (MTG), and Shunyi (SY) meteorological stations, which represent the south, east, west, and north areas of Beijing, respectively. It was shown that the temporal variation in simulated wind speed at the four stations were consistent with the observations from the perspective of time serial of wind speed, but the simulations were higher than the observations due to impacts of the complex topography and limited observation data assimilated to the LAPS-WRF model (Fig. S2 and Fig. S4a). To calculate the E_{NOX} accurately, we corrected the simulated wind speed using the observation data from the four weather stations in order to reduce the systemic error. Specifically, we computed the relative error of the modeled wind speed based on measurements at four weather stations for each journey and then added the error bar to simulated wind speed at every sampling position during the same journey. The correlation coefficient between simulated and observed wind speeds at the four stations is 0.47, and the result passesthe 99.9% significance test. The root mean square error (RMSE) is small, with a value of 1.18 m s^{-1}. Except for the MTG station, simulated wind directions at the other three stations are in accordance with the observations, particularly for the primary wind direction (Fig. S3 and Fig.S4b). In general, simulated wind direction are also coincident with observations from the perspective of time serial of wind direction, and simulations are larger than measurements during some periods at some stations due to the effects of the complex topography and limited observation data assimilated to the model (Fig.S4b). The primary wind direction and its frequency at the MTG station are not consistent with the observations because these are affected by the complex topography near the Taihang and Yanshan mountains. In general, the corrected wind speed and wind direction data are reliable for estimation of the NO$_X$ emissions, and the uncertainty of E_{NOX} due to the variation of wind field will be discussed in Section 3.3.

Figure S4 presents the temporal variation in simulated and observed NO₂ concentration from January 18 to October 13, 2014. The hourly measurements of NO₂ concentrations (shown in Fig. S1b) were obtained from the National Environment Monitoring Station in China. In general, the temporal variation in the NO₂ simulation is consistent with the observation. The simulated values are close to the

320   observations, except for January 21–24, September 19, and October 9–10, when NO_2 simulations are

higher than the observations. The correlation coefficient between simulated and observed NO_2

concentrations is 0.73, and the result passes the 99.9% significance test (Fig. S5). The RMSE and mean

absolute error (MAE) are 16.14 and 19.21 μg m^{-3}, respectively. The observed NO_2 might include some

NO_z component, leading to a systematical biases (underestimation) of NO_2 by model compared to

325   observation (Ma et al., 2012). Thus, the simulated NO_2 concentrations and hence the ratio of NO_2 and

NO_x are reliable for estimating NO_X emissions.

2.4 Selection of the journeys for estimating NOx emissions

To estimate the NO_2 fluxes (F_{NO2}) and E_{NOX} accurately, we firstly selected six journeys with the RMSEs

of simulated wind speeds at the four weather stations smaller than 1.5 m s^{-1} from the primary selected 11

330   journeys. Then we assessed whether the meteorological and chemical conditions meet the criteria of

Shaiganfar et al. (2017) for each of these six journeys. It should be pointed out that we cannot assess the

problem of large partitioning ratio due to the absence of the whole seasonal simulated or observed data

in autumn and winter. The assessment results of other four problems are listed in Table 2. We excluded

the journeys in which more than two problems occurred. It needs to be noted that lifetime correction

335   coefficients c_{τ} on October 12 and 13 are slightly larger than 1.5, which is the criteria of large lifetime

correction (Shaiganfar et al., 2017), so we also adopted the data on October 12 and 13 to estimate the

E_{NOX}. Lastly, NO_2 VCD measurements outside of the 6th Ring Rd during five selected journeys were not

used to quantify F_{NO2} and E_{NOX}.

3.   Results and discussion

340   **3.1 Tropospheric NO$_2$ VCD**

Figure 4 presents the journey-to-journey temporal variation in the tropospheric NO_2 VCD on the 6th Ring

Rd of Beijing in January, September, and October, 2014. In general, the NO_2 VCD in January was higher

than that in other months. The highest values occurred on January 19, 23, and 24. The mean NO_2 VCD

ranged mostly from 4.5±1.83 × 10^{16} to 9.0±1.24 × 10^{16} molecules cm^{-2} in January, but values were all

345   lower than 4.5 × 10^{16} molecules cm^{-2} in September and October. The NO_2 VCD values during the

mornings of January 23 and October 13 were 9.05 × 10^{16} and 1.23 × 10^{16} molecules cm^{-2}, corresponding

to the maximum and minimum values, respectively, during the 19 circling journeys. This result might be

caused by higher emissions from coal fired heating (Table S1) and lower photolysis of NO_2 in winter. A similar pattern of seasonal variation in tropospheric NO_2 VCD was found previously by site MAX-DOAS measurements in Beijing(Ma et al., 2013a;Hendrick et al., 2014).

To investigate the differences in the spatial distribution of NO_2 VCD among the three months, we computed the monthly average NO_2 VCD for every sampling point along the 6th Ring Rd of Beijing in January, September, and October, 2014. Firstly, we used the locations of all sampling points on the morning of September 23 as the reference point for the calculation of NO_2 VCD monthly average, with the most sampling sites (98 points) for all observation periods. Then, we calculated the monthly average value at each reference point using the data of the nearest sampling point. The distance from the nearest sampling point to a reference point was less than 1.5 km. Figure 5 shows that the monthly average NO_2 VCD values at most sampling points on the 6th Ring Rd were obviously larger in January than in other two months (by a factor of two in most cases). The spatial distribution characteristics of NO_2 VCD in September were similar to those in October. In addition, the NO_2 VCD values at the northern and southern parts of the 6th Ring Rd were all larger than those in other areas for all three months. The high NO_2 VCD in the southern region was related to strong local emissions to the south of Beijing and transport from central and southern Hebei and the city of Tianjin (Meng et al., 2018).. As shown in Fig. 4, the maximum journey-averaged NO_2 VCD occurred on the morning of January 23, and the minimum occurred on the morning of October 13.

We investigated the spatial distribution differences in NO_2 VCD between these two circling journeys, as shown in Fig. 6. The NO_2 VCD values on the 6th Ring Rd in the morning of January 23 were all large, particularly in the north and southwest areas, with magnitudes of 10×10^{16} to 12×10^{16} molecules cm^{-2}. On October 13, high NO_2 VCD was located at the southern areas and it might be related to the southern emission sources closer to the south 6th Ring Rd, which its emission rates are obviously higher than the north Ring Rd. The spatial distribution differences between these two journeys were related to the high emission during the heating season in January (see section 3.2) and the impacts of the wind field. We used thin-grid ECWMF reanalysis data for January 23 and October 13 with a spatial resolution of $0.125°$ $\times 0.125°$ to investigate the impact of the wind field on the spatial distribution of NO_2 VCD. Figure 7 shows the wind fields at 8:00 and 14:00 BJT on these two days, respectively. The NO_2 VCD was large with weak south wind and convergence of southeast and northwest wind in Beijing and its surrounding area, but its values were far smaller with strong north wind. Weak south wind and a breeze or calm wind

resulted in the transport of NO_2 from the south area in Hebei Province and its accumulation on January

23. Strong north wind suppressed the transport of NO_2 from the south area on October 13. These results

380   indicate that the wind field has large impacts on the spatial distribution of NO_2 VCD in Beijing.

Figure 8 presents the spatial distributions of wind and NO_2 VCD averaged for the two different wind

fields. The mean NO_2 VCD at most sampling points along the 6th Ring Rd was obviously higher under

the south wind field than under the north wind. High NO_2 emission sources were located within the 5th

Ring Rd of Beijing in the three months (Fig. 10), and the background concentrations of NO_2 VCD in the

385   north and south areas were remarkably different due to the impacts of emission sources to the south of

Beijing. Hence, southerly wind can transfer air pollutants from the southern area to Beijing and lead to

high NO_2 flux, whereas impacts of north wind on NO_2 flux are smaller because the background

concentration of NO_2 VCD to the north of Beijing were lower. Convergence of the wind field in the south

parts of the 6th Ring Rd is favorable to the accumulation of NO_2 from the surrounding area to the southern

390   parts of the ring road.

3.2 Quantification of NOx emissions

Figure 9 shows the journey-to-journey variation in estimated F_{NO2} and E_{NOX} over Beijing for five circling

journeys in January, September, and October, 2014. The F_{NO2} fell in between 1.85×10^{25} and 15.67×10^{25}

molecules s^{-1}. The ranges of E_{NOX} during the heating (January) and non-heating (September and October)

395   periods were 22.59×10^{25} to 31.28×10^{25} molecules s^{-1} and 9.61×10^{25} to 11.96×10^{25} molecules s^{-1},

respectively. The average E_{NOX} values in the heating and non-heating periods were $26.94 \pm 6.14 \times 10^{25}$

molecules s^{-1} and $10.99 \pm 1.23 \times 10^{25}$ molecules s^{-1}, respectively. In general, the journey-to-journey

variation patterns of F_{NO2} and E_{NOX} are consistent with that of the mean NO_2 VCD. In other words, the

estimate of E_{NOX} is determined mainly by the NO_2 VCD. Seasonal variation characteristics of the

400   estimated E_{NOX} were obvious. Specifically, the total E_{NOX} was higher in January than in the other two

months. The average E_{NOX} in the heating period was about 2.5 times as much as those in the non-heating

period. The coal fired heating in Beijing included central heating in urban area and scattered coal

combustion in suburb or rural area for the year 2014. We calculated the average NO_X emission rates of

four sectors including industry, power, residential, and transportation from the MEIC within the 6th Ring

405   Rd of Beijing in January, September, and October 2012, and the ratio of each specific NO_X emission rate

in January to the corresponding average value in September and October (Table S1). The E_{NOX} from the

power and residential section were remarkably higher in January than in other two months, and especially E_{NOX} from the residential was about 5 times more in January than in other months. In general, central heating in urban area are from power plant and residential use the scattered coal combustion in suburb or rural area.

In addition to the seasonal differences, the journey-to-journey variation in estimated E_{NOX} is large even within the same month, mainly due to uncertainties in the calculations of wind speed, ratio of NO_2 and NOx concentration, and decay rate of NO_X from the emission sources to the measured positions under different meteorological conditions. In addition to the NO_2 VCD, wind speed, and wind direction at the sampling points, the estimated NO_X emission rate is obviously affected by the Leighton ratio of NO and NO_2 concentration and the lifetime of NOx (Valin, et al., 2013). Thus, the estimated NO_X emission rate could be very large even if the NO_2 VCD was small, such as in the case of September 14. It should be noted that the low mean wind speed on September 14 leads to high c_τ, so the E_{NOX} for this journey is not so low although the F_{NO2} was very low. In addition, if both c_τ and c_L are large, high E_{NOX} can be derived.

3.3 Comparisons with MEIC inventory and other estimates

We compared the estimated NO_X emission with the multi-resolution emission inventory in China (MEIC) released by Tsinghua University for 2012 (MEIC 2012) (Zhang et al., 2009;Zhang et al., 2012). The horizontal resolution of MEIC 2012 is $0.25° \times 0.25°$, and five sectors, i.e., agriculture, industry, power, residential, and transportation, are included.

Figure 10 presents the spatial distributions of NO_X emission rates over Beijing in January, September, and October, 2012, from MEIC. A high NO_X emission zone was located within the 5th Ring Rd of Beijing, and low emissions occurred in its surroundings. The NO_X emissions in January were obviously larger than those in the other two months.

Figure 11 shows the estimated NO_x emission rates from Car MAX-DOAS measurements for each selected journey (see Sect. 2.4) in January, September, and October, 2014, and the corresponding monthly averaged NO_x emission rates from the MEIC 2012 for the same region within the 6th Ring Rd of Beijing (hereafter expressed as MEIC_Month). The MEIC_Month is obviously lower than the estimated E_{NOX} in January. While the two emission estimates are very close in September, the MEIC_Month is slightly smaller than the E_{NOX} in October. The differences between the estimated E_{NOX} and the MEIC_Month

during some journeys were remarkably large. The differences between the E_{NOX} and MEIC 2012 during the 10 journeys may be caused by (1) the interannual variations in emission inventory, (2) the different timescales of the two emission estimates, (3) the uncertainty of the estimated E_{NOX} and MEIC 2012. Firstly, the E_{NOX} in this study is estimated for the year 2014, whereas the MEIC_Month was established for the year 2012. Secondly, our results represent only the conditions during a few measurements during daytime, whereas the MIEC 2012 denoted monthly average conditions. Thirdly, the uncertainty of MEIC 2012 is large, particularly in autumn and winter (Li *et al*., 2017; Meng *et al*., 2018). There are also large uncertainties in the estimated E_{NOX} caused by, e.g., the inconsistency of wind field during a circling journey and the transfer of NO_2 from other source areas than urban Beijing. The CIM assumes that the wind field is constant during the of measurements period and that the wind speed is also sufficiently high. However, the wind field during some journeys (January 27 and October 12,13) might have changed systematically. Ibrahim *et al*. (2010) also pointed out that systematic changes during the measurements period can have large impacts on the emission estimate, particularly if measurements with high trace gas VCD are accompanied by strong deviations of the actual wind speed (or direction) from the assumed average values. For example, on the afternoon of January 27, high NO_2 VCD was measured, and the wind field changed during the measurement journey. In such cases, the systematic changes in wind speed and direction can lead to additional uncertainties in E_{NOX}. Moreover because the southerly wind can bring NO_x emitted in the south-central regions of Hebei Province to Beijing, the E_{NOX} from Car MAX-DOAS measurements will be overestimated under south wind conditions, e.g., on January 26.

3.4 Uncertainty analysis of estimated emissions.

We calculated the uncertainty of E_{NOX} according to the error transfer formula of relative deviation based on the errors of measured NO_2 VCD, simulated wind speed and direction, and c_L and c_τ. The standard deviation (STD) of wind speed over a period of time can provide a bound for the related uncertainties of the emission estimate (Ibrahim *et al*., 2010). Therefore, we first computed the uncertainty of F_{NO2} based on the STD of simulated wind speed after correction and the measurement error of NO_2 VCD (about $\pm$ 10%, Ma *et al*., 2013a) for each journey. Then, we calculated STD of c_τ according to the first derivative of equation (4) and the STD of c_L using different NOx lifetime and the ratios of NO_X and NO_2 at sampling position on the 6th Ring Rd of Beijing for each journey. Figure 11 shows the uncertainties of E_{NOX} for five journeys and the uncertainty range of E_{NOX} is 2.23×10^{25} to 9.12×10^{25}

465   molecules s^{-1} (19.52–52.01%).

We also give the spatial variation in the NO$_X$/NO$_2$ ratio and NO$_X$ lifetime at the entire route for the emission calculation during five journeys (Fig. S7 and S8), and estimate the error contribution of five factors including NO$_2$ VCD, wind speed, wind direction, the NO$_X$/NO$_2$ ratio, and the NO$_X$ lifetime to the total uncertainty of E$_{NOX}$ (Table 3). In general, there are obvious seasonal and regional difference in the

470   NO$_X$/NO$_2$ ratio and NO$_X$ lifetime and it is necessary to use specific ratios and lifetime value to estimate the E$_{NOX}$ for each journey. Specifically, the NO$_X$/NO$_2$ ratio and NO$_X$ lifetime are larger in January than in September and October, and they are larger at the southern part of the 6th Ring Rd than at other parts for most journeys. Among error contributions of five factors, the impacts of wind speed and direction are the largest for most journeys except for September 14. For January 26 and 27, error contributions of wind

475   speed to the uncertainty of E$_{NOX}$ are larger than other four factors. For September 14, uncertainty of E$_{NOX}$ is mainly caused by the errors of NOx lifetime and wind direction. For October 12 and 13, error contributions of the NO$_X$/NO$_2$ ratio are also remarkable. Thus, it is important to obtain the accurate wind vector profiles, NO$_X$, NO$_2$, and OH concentration data except for NO$_2$ VCD to reduce the uncertainty of E$_{NOX}$ estimation using the CIM.

480   We also calculate the Leighton ratios, L_r, to assess impacts of VOCs on the NOx lifetime. The L_r during five journeys is 0.85, 0.80, 1.04, 1.19, and 1.33 on January 26 and 27, September 14, October 12 and 13, respectively. Results show that the NOx lifetime for the three journeys on September and October are affected by VOCs and lead to extra errors of E$_{NOX}$. While VOCs can't cause the deviation in the NOx lifetime and estimation of the E$_{NOX}$ in January.

485

4.   Conclusions

We carried out 19 city-circle-around Car MAX-DOAS experiments on the 6th Ring Rd of Beijing in January, September, and October, 2014. The VCD of NO$_2$ was retrieved and the temporal and spatial distributions were investigated. Then the NO$_X$ emission rates in urban Beijing were estimated using the

490   measured NO$_2$ VCD together with the refined wind fields, NO$_2$ to NOx ratios, and NO$_2$ lifetimes simulated by the LAPS-WRF-CMAQ model system, and the results were compared to the emission rates from the MEIC inventory 2012.

The NO$_2$ VCD values averaged for each experimental journey in January were all larger than those in the other two months, mainly due to higher emissions in winter. The measured NO$_2$ VCD was typically

495 larger at the southern parts of the 6th Ring Road than at the northern parts because weak south wind

resulted in the transport and accumulation of NO_2 from southern areas in Hebei Province and strong north

wind suppressed the transport of NO_2 from the southern area. Such inhomogeneous distributions of

tropospheric NO_2 VCD bring a challenge for the validation of satellite products for Beijing as well as

other megacities.

500 The journey-to-journey variation in estimated E_{NOX} were large, even within the same month, mainly

due to uncertainties in the calculation of wind speed, the ratio of NO_2 and NOx concentration, and the

decay rate of NO_X from the emission sources to the measured positions under different meteorological

conditions. The average E_{NOX} values in the heating and non-heating periods are estimated to be $26.94\pm$

6.14×10^{25} molecules s^{-1} and $10.99\pm1.23 \times 10^{25}$ molecules s^{-1}, respectively, with an uncertainty range

505 of 19.52–52.01%. The monthly emission rates in the area within the 6th Ring Rd of Beijing from MEIC

2012 are lower than the estimated E_{NOX}, particularly in January. The differences between the E_{NOX} and

the monthly emission rates from MEIC 2012 can be attributed to the interannual differences in the

emissions inventory, the different timescales and uncertainties of two kinds of inventory.

Our results show that Car MAX-DOAS measurements can be used effectively for dynamic monitoring

510 and updating of the NO_x emissions from megacities such as Beijing. To estimate the E_{NOX} by Car MAX-

DOAS accurately in Beijing and other similar megacities, appropriate meteorological conditions, such

as small fluctuations of the wind field, relatively larger wind speed, and suitable wind direction, need to

be selected to avoid the impact of extra transfers of large emission sources from surrounding areas. In

addition to the NO_2 VCD, simultaneous observations of wind speed, wind direction, and surface NO and

515 NO_2 concentrations are recommended to reduce the uncertainties of E_{NOX} .

Data availability. The NCEP-FNL reanalysis and ECMWF are publicly available at

http://rda.ucar.edu/datasets/ds083.2/ and https://www.ecmwf.int/en/forecasts/datasets , respectively. The

NO_2 measurements and meteorological observations including wind speed and wind direction data are

520 available at http://113.108.142.147:20035/emcpublish and http://data.cma.cn/, respectively. The

tropospheric NO_2 VCD data derived from this study are available on the request.

Author contributions. JM and XC designed the research. JM, JJ, JG, MQ, QX, and PY contributed to the

measurements, and JM performed the spectral analysis and retrieval. XC and JP designed the model

525 experiment and performed the model simulations. XC, YL, JP, and XM contributed to the data processing

and analyses. XC and JM analyzed the results and wrote the paper with inputs from all authors.

Competing interests. The authors declare that they have no conflicts of interest.

530 *Acknowledgments*. This work was supported jointly by the National Natural Science Foundation of China

(91644223), the National Research Program for Key Issues in Air Pollution Control (DQGG0104), and

the Scientific and Technological Development Funds from the Chinese Academy of Meteorological

Sciences (2018KJ042). The authors acknowledge Tsinghua University for providing the emissions

inventory and the China National Environmental Monitoring Centre for providing surface NO_2

535 observation data.

References

Albers, S. C., McGinley, J. A., Birkenheuer, D., and Smart, J. R.: The local analysis and prediction system

(LAPS): Analyses of clouds, precipitation, and temperature, Wea. Forecasting, 11, 273-287, 1996.

Brinksma, E. J., Pinardi, G., Volten, H., Braak, R., Richter, A., Schoenhardt, A., van Roozendael, M.,

540 Fayt, C., Hermans, C., Dirksen, R. J., Vlemmix, T., Berkhout, A. J. C., Swart, D. P. J., Oetjen, H.,

Wittrock, F., Wagner, T., Ibrahim, O. W., de Leeuw, G., Moerman, M., Curier, R. L., Celarier, E. A.,

Cede, A., Knap, W. H., Veefkind, J. P., Eskes, H. J., Allaart, M., Rothe, R., Piters, A. J. M. and Levelt,

P. F.: The 2005 and 2006 DANDELIONS NO2 and aerosol intercomparison campaigns, J. Geophys.

Res.-Atmospheres, 113(D16), D16S46, doi:10.1029/2007JD008808, 2008.

545 Burrows, J. P., Richter, A., Dehn, A., Deters, B., Himmelmann, S., Voigt, S., and Orphal, J.: Atmospheric

remote sensing reference data from GOME-2. temperature-dependent absorption cross-sections of O_3

in the 231-794 nm range, J. Quant. Spectrosc. Ra., 61, 509-517, 1999.

Cao, C., Jiang, W., Wang, B., Fang, J., Lang, J., Tian, G., Jiang, J., and Zhu, T. F.: Inhalable

microorganisms in Beijing's $PM_{2.5}$ and PM_{10} pollutants during a severe smog event, Environ Sci

550 Technol, 48, 1499-1507, 10.1021/es4048472, 2014.

Cheng, X., Sun, Z., Li, D., Xu, X., Jia, M., and Cheng, S.: Short-term aerosol radiative effects and their

regional difference during heavy haze episodes in January 2013 in China, Atmospheric Environment,

165, 248-263, 10.1016/j.atmosenv.2017.06.040, 2017.

Davis, Z. Y. W., Baray, S., McLinden, C. A., Khanbabakhani, A., Fujs, W., Csukat, C., Debosz, J. and McLaren, R.: Estimation of NOx and SO2 emissions from Sarnia, Ontario, using a mobile MAX-DOAS (Multi-AXis Differential Optical Absorption Spectroscopy) and a NOx analyzer, Atmospheric Chem. Phys., 19(22), 13871–13889, doi:https://doi.org/10.5194/acp-19-13871-2019, 2019.

Dennis, R., Byun, D., and Novak, J.: The next generation of integrated air quality modeling: EPA's Models-3, Atmos. Environ., 30, 1925-1938, 1996.

Dickerson, R. R., Stedman, D. H., and Delany, A. C.: Direct measurements of ozone and nitrogen dioxide photolysis rates in the troposphere, Journal of Geophysical Research, 87, 10.1029/JC087iC07p04933, 1982.

Fayt, C., and Van Roozendael, M.: WinDOAS 2.1 software user manual, IASB/BIRA Uccle, Belgium, 2011.

Greenblatt, G. D., Orlando, J. J., Burkholder, J. B., and Ravishankara, A. R.: Absorption measurements of oxygen between 330 and 1140 nm, J. Geophys. Res., 95, 18577-18582, 10.1029/JD095iD11p18577, 1990.

Hönninger, G. and Platt, U.: Observations of BrO and its vertical distribution during surface ozone depletion at Alert, Atmos. Environ., 36, 2481–2489, https://doi.org/10.1016/S1352-2310(02)00104-8, 2002.

Hönninger, G., von Friedeburg, C., and Platt, U.: Multi axis differential optical absorption spectroscopy (MAX-DOAS), Atmos. Chem. Phys., 4, 231-254, 10.5194/acp-4-231-2004, 2004.

Hao, J., Tian, H., and Lu, Y.: Emission inventories of NOX from commercial energy consumption in China, 1995-1998, Environmental Science and Technology, 36, 552–560, 2002.

He, H., Wang, X. M., Wang, Y. S., Wang, Z. F., Liu, J. G., and Chen, Y. F.: Formation Mechanism and Control Strategies of Haze in China, Bull. Chin. Acad. Sci., 28, 344-352, 2013.

Hendrick, F., Müller, J. F., Clémer, K., Wang, P., De Mazière, M., Fayt, C., Gielen, C., Hermans, C., Ma, J. Z., Pinardi, G., Stavrakou, T., Vlemmix, T., and Van Roozendael, M.: Four years of ground-based MAX-DOAS observations of HONO and NO2 in the Beijing area, Atmospheric Chemistry and Physics, 14, 765-781, 10.5194/acp-14-765-2014, 2014.

Huang, R. J., Zhang, Y., Bozzetti, C., Ho, K. F., Cao, J. J., Han, Y., Daellenbach, K. R., Slowik, J. G., Platt, S. M., Canonaco, F., Zotter, P., Wolf, R., Pieber, S. M., Bruns, E. A., Crippa, M., Ciarelli, G., Piazzalunga, A., Schwikowski, M., Abbaszade, G., Schnelle-Kreis, J., Zimmermann, R., An, Z., Szidat, S., Baltensperger, U., El Haddad, I., and Prevot, A. S.: High secondary aerosol contribution to

585   particulate pollution during haze events in China, Nature, 514, 218-222, 10.1038/nature13774, 2014.

Ibrahim, O., Shaiganfar, R., Sinreich, R., Stein, T., Platt, U., and Wagner, T.: Car MAX-DOAS measurements around entire cities: quantification of NO_x emissions from the cities of Mannheim and Ludwigshafen (Germany), Atmos. Meas. Tech., 3, 709-721, 10.5194/amt-3-709-2010, 2010.

Irie, H., Kanaya, Y., Akimoto, H., Z., W., Gleason, J. F., and Bucsela, E. J.: Validation of OMI

590   tropospheric NO2 column data using MAX-DOAS measurements deep inside the North China Plain in June 2006 Mount Tai Experiment 2006, Atmos. Chem. Phys., 8, 6577-6586, 2008.

Jaegle', L., Steinberger, L., Martin, R. V., and Chance, K.: Global partitioning of NOX sources using satellite observations: relative roles of fossil fuel combustion, biomass burning and soil emissions, The Royal Society of Chemistry, 130, 407–423, 2005.

595   Jin, J., Ma, J., Lin, W., Zhao, H., Shaiganfar, R., Beirle, S., and Wagner, T.: MAX-DOAS measurements and satellite validation of tropospheric NO2 and SO2 vertical column densities at a rural site of North China, Atmospheric Environment, 133, 12-25, http://dx.doi.org/10.1016/j.atmosenv.2016.03.031, 2016.

Johansson, M., Galle, B., Yu, T., Tang, L., Chen, D., Li, H., Li, J. X., and Zhang, Y.: Quantification of

600   total emission of air pollutants from Beijing using mobile mini-DOAS, Atmospheric Environment, 42, 6926-6933, http://dx.doi.org/10.1016/j.atmosenv.2008.05.025, 2008.

Johansson, M., Rivera, C., de Foy, B., Lei, W., Song, J., Zhang, Y., Galle, B., and Molina, L.: Mobile mini-DOAS measurement of the outflow of NO2 and HCHO from Mexico City, Atmos. Chem. Phys., 9, 5647-5653, 10.5194/acp-9-5647-2009, 2009.

605   Konovalov, I. B., Beekmann, M., Richter, A., and Burrows, J. P.: Inverse modeling of the spatial distribution of NOX emissions on a continental scale using satellite data, Atmospheric Chemistry and Physics, 6, 1747-1770, 2006.

Kraus, S.: DOASIS, DOAS for Windows software [CD-ROM], in: Proceedings of the 1st International DOAS-Workshop, Heidelberg, Germany, 13-14 September 2001, 2001a.

610   Kraus, S.: DOASIS, DOAS for Windows software [CD-ROM], in: Proceedings of the 1st International DOAS-Workshop, Heidelberg,Germany,13–14 September 2001, 2001b.

Li, M., Liu, H., Geng, G., Hong, C., Liu, F., Song, Y., Tong, D., Zheng, B., Cui, H., Man, H., Zhang, Q., and He, K.: Anthropogenic emission inventories in China: a review, National Science Review, 4, 834-866, 10.1093/nsr/nwx150, 2017.

615   Li, X., Brauers, T., Hofzumahaus, A., Lu, K., Li, Y., Shao, M., Wagner, T., and Wahner, A.: MAX-DOAS measurements of NO2, HCHO and CHOCHO at a rural site in Southern China, Atmospheric Chemistry and Physics, 13, 2133-2151, 2013.

Liao, L., Lou, S. J., Fu, Y., Chang, W. J., and Liao, H.: Radiative forcing of aerosols and its impact on surface air temperature on the synoptic scale in eastern China, Chin. J. Atmos. Sci. (Chin. Ver.), 39,

620   68-82, 2015.

Lin, J. T., Liu, Z., Zhang, Q., Liu, H., Mao, J., and Zhuang, G.: Modeling uncertainties for tropospheric nitrogen dioxide columns affecting satellite-based inverse modeling of nitrogen oxides emissions, Atmospheric Chemistry and Physics, 12, 12255-12275, 10.5194/acp-12-12255-2012, 2012.

Ma, J., and Van Aardenne, J. A.: Impact of different emission inventories on simulated tropospheric ozone

625   over China: a regional chemical transport model evaluation, Atmos. Chem. Phys., 4, 877-887, 2004.

Ma, J. Z., Wang, W., Chen, Y., Liu, H. J., Yan, P., Ding, G. A., Wang, M. L., Sun, J., and Lelieveld, J.: The IPAC-NC field campaign: a pollution and oxidization pool in the lower atmosphere over Huabei, China, Atmos. Chem. Phys., 12, 3883-3908, 10.5194/acp-12-3883-2012, 2012.

Ma, J., Wang, W., Liu, H., Chen, Y., Xu, X., and Lelieveld, J.: Pollution plumes observed by aircraft over

630   North China during the IPAC-NC field campaign, Chinese Science Bulletin, 58, 4329-4336, 10.1007/s11434-013-5978-9, 2013.

Ma, J. Z., Beirle, S., Jin, J. L., Shaiganfar, R., Yan, P., and Wagner, T.: Tropospheric NO_2 vertical column densities over Beijing: results of the first three years of ground-based MAX-DOAS measurements (2008–2011) and satellite validation, Atmospheric Chemistry and Physics, 13,

635   1547-1567, 10.5194/acp-13-1547-2013, 2013a.

Martin, R. V.: An improved retrieval of tropospheric nitrogen dioxide from GOME, Journal of Geophysical Research, 107, 10.1029/2001jd001027, 2002.

McGinley, J. A., Albers, S., and Stamus, P.: Validation of a composite convective index as defined by a real-time local analysis system, Wea.Forecasting, 6, 337-356, 1991.

640   Meng, K., Xu, X., Cheng, X., Xu, X., Qu, X., Zhu, W., Ma, C., Yang, Y., and Zhao, Y.: Spatio-temporal variations in SO2 and NO2 emissions caused by heating over the Beijing-Tianjin-Hebei Region constrained by an adaptive nudging method with OMI data, The Science of the total environment, 642, 543-552, 10.1016/j.scitotenv.2018.06.021, 2018.

Michalakes, J., Dudhia, J., Gill, D., Henderson, T., Klemp, J., Skamarock, W., and Wang, W.: The weather

645   research and forecast model: software architecture and performance, the 11th ECMWFWorkshop on

the Use of High Performance Computing In Meteorology, George Mozdzynski, 2004.

Otte, T. L., and Pleim, J. E.: The Meteorology-Chemistry Interface Processor (MCIP) for the CMAQ

modeling system: updates through MCIPv3.4.1, Geosci. Model Dev., 3, 243-256, 2010.

Platt, U.: Differential optical absorption spectroscopy (DOAS), in: Air Monitoring by Spectroscopic

650   Techniques, edited by: Sigrist, M. W., Chemical Analysis Series, 127, John Wiley, New York, 27–84,

1994.

Platt, U., and Stutz, J.: Differential Optical Absorption Spectroscopy Principles and Applications, Physics

of Earth and Space Environments, Springer, Heidelberg, 2008.

Shaiganfar, R., Beirle, S., Sharma, M., Chauhan, A., Singh, R. P., and Wagner, T.: Estimation of NO_x

655   emissions from Delhi using Car MAX-DOAS observations and comparison with OMI satellite data,

Atmos. Chem. Phys., 11, 10871-10887, 10.5194/acp-11-10871-2011, 2011.

Shaiganfar, R., Beirle, S., van der Gon, H. D., Jonkers, S., Kuenen, J., Petetin, H., Zhang, Q., Beekmann,

M. and Wagner, T.: Estimation of the Paris NOx emissions from mobile MAX-DOAS observations

and CHIMERE model simulations during the MEGAPOLI campaign using the closed integral method,

660   Atmospheric Chem. Phys., 17(12), 7853–7890, doi:10.5194/acp-17-7853-2017, 2017.

Streets, D. G., Canty, T., Carmichael, G. R., de Foy, B., Dickerson, R. R., Duncan, B. N., Edwards, D. P.,

Haynes, J. A., Henze, D. K., Houyoux, M. R., Jacob, D. J., Krotkov, N. A., Lamsal, L. N., Liu, Y., Lu,

Z., Martin, R. V., Pfister, G. G., Pinder, R. W., Salawitch, R. J., and Wecht, K. J.: Emissions estimation

from satellite retrievals: A review of current capability, Atmospheric Environment, 77, 1011-1042,

665   10.1016/j.atmosenv.2013.05.051, 2013.

Tan, T., Hu, M., Li, M., Guo, Q., Wu, Y., Fang, X., Gu, F., Wang, Y., and Wu, Z.: New insight into $PM_{2.5}$

pollution patterns in Beijing based on one-year measurement of chemical compositions, The Science

of the total environment, 621, 734-743, 10.1016/j.scitotenv.2017.11.208, 2018.

UNC: SMOKE v3.6 user's manual, Chapel Hill: The institute for the Environmen, 2014.

670   Vandaele, A. C., Hermans, C., Simon, P. C., Carleer, M., Colin, R., Fally, S., Mérienne, M. F.,

Jenouvrier, A., and Coquart, B.: Measurements of the NO_2 absorption cross-section from 42 000 cm^{-1}

to 10 000 cm^{-1} (238–1000 nm) at 220 K and 294 K, J. Quant. Spectrosc. Ra., 59, 171-184, 1998.

Valin, L. C., Russell, A. R. and Cohen, R. C.: Variations of OH radical in an urban plume inferred from

NO2 column measurements, Geophys. Res. Lett., 40(9), 1856–1860, doi:10.1002/grl.50267, 2013.

675 Vlemmix, T., Piters, A., Stammes, P., Wang, P., and Levelt, P.: Retrieval of tropospheric NO2 using the MAX-DOAS method combined with relative intensity measurements for aerosol correction, Atmospheric Measurement Techniques, 3, 1287-1305, 2010.

Wagner, T., Dix, B., Friedeburg, C. v., Frieß, U., Sanghavi, S., Sinreich, R., and Platt, U.: MAX-DOAS O_4 measurements: A new technique to derive information on atmospheric aerosols -- Principles and

680 information content, J. Geophys. Res., 109, D22205, 10.1029/2004jd004904, 2004.

Wagner, T., Ibrahim, O., Shaiganfar, R., and Platt, U.: Mobile MAX-DOAS observations of tropospheric trace gases, Atmos. Meas. Tech., 3, 129-140, 2010a.

Wagner, T., Ibrahim, O., Shaiganfar, R., and Platt, U.: Mobile MAX-DOAS observations of tropospheric trace gases, Atmos. Meas. Tech., 3, 129-140, 10.5194/amt-3-129-2010, 2010b.

685 Wagner, T., Beirle, S., Brauers, T., Deutschmann, T., Frieß, U., Hak, C., Halla, J. D., Heue, K. P., Junkermann, W., Li, X., Platt, U., and Pundt-Gruber, I.: Inversion of tropospheric profiles of aerosol extinction and HCHO and NO_2; mixing ratios from MAX-DOAS observations in Milano during the summer of 2003 and comparison with independent data sets, Atmospheric Measurement Techniques, 4, 2685-2715, 10.5194/amt-4-2685-2011, 2011.

690 Wang, S., Zhou, B., Wang, Z., Yang, S., Hao, N., Valks, P., Trautmann, T., and Chen, L.: Remote sensing of NO2 emission from the central urban area of Shanghai (China) using the mobile DOAS technique, Journal of Geophysical Research: Atmospheres, 117, D13305, 10.1029/2011jd016983, 2012.

Wang, Y., McElroy, M. B., Martin, R. V., Streets, D. G., Zhang, Q., and Fu, T.-M.: Seasonal variability of NOxemissions over east China constrained by satellite observations: Implications for combustion

695 and microbial sources, Journal of Geophysical Research, 112, 10.1029/2006jd007538, 2007.

Wittrock, F., Oetjen, H., Richter, A., Fietkau, S., Medeke, T., Rozanov, A., and Burrows, J.: MAX-DOAS measurements of atmospheric trace gases in Ny-Ålesund-Radiative transfer studies and their application, Atmos. Chem. Phys., 4, 955-966, 2004.

Wu, F., Xie, P., Li, A., Mou, F., Chen, H., Zhu, Y., Zhu, T., Liu, J., and Liu, W.: Investigations of temporal

700 and spatial distribution of precursors SO_2 and NO_2; vertical columns in the North China Plain using mobile DOAS, Atmospheric Chemistry and Physics, 18, 1535-1554, 10.5194/acp-18-1535-2018, 2018.

Zhang, Q., Streets, D. G., He, K., Wang, Y., Richter, A., Burrows, J. P., Uno, I., Jang, C. J., Chen, D., Yao, Z., and Lei, Y.: NOxemission trends for China, 1995–2004: The view from the ground and the view from space, Journal of Geophysical Research, 112, 10.1029/2007jd008684, 2007.

705 Zhang, Q., Streets, D. G., Carmichael, G. R., He, K. B., Huo, H., Kannari, A., Klimont, Z., Park, I. S.,

Reddy, S., Fu, J. S., Chen, D., Duan, L., Lei, Y., Wang, L. T., and Yao, Z. L.: Asian emissions in 2006 for the NASA INTEX-B mission, Atmos. Chem. Phys., 9, 5131-5153, 2009.

Zhang, Q., Geng, G., Wang, S., Richter, A., and He, K.: Satellite remote sensing of changes in NOx emissions over China during 1996–2010, Chinese Science Bulletin, 57, 2857-2864, 10.1007/s11434-012-5015-4, 2012.

Zhang, X. Y., Sun, J. Y., Wang, Y. Q., Li, W. J., Zhang, Q., Wang, W. G., Quan, J. N., Cao, G. L., Wang, J. Z., Yang, Y. Q., and Zhang, Y. M.: Factors contributing to haze and fog in China, Chin. Sci. Bull. (Chin. Ver.), 58, 1178-1187, 2013.

Zhao, B., Wang, P., Ma, J. Z., Zhu, S., Pozzer, A., and Li, W.: A high-resolution emission inventory of primary pollutants for the Huabei region, China, Atmospheric Chemistry and Physics, 12, 481-501, 10.5194/acp-12-481-2012, 2012.

Zyrichidou, I., Koukouli, M. E., Balis, D., Markakis, K., Poupkou, A., Katragkou, E., Kioutsioukis, I., Melas, D., Boersma, K. F., and van Roozendael, M.: Identification of surface NOx emission sources on a regional scale using OMI NO2, Atmospheric Environment, 101, 82-93, 10.1016/j.atmosenv.2014.11.023, 2015.

710

715

720

725

730

735

Table 1. Sampling periods of the Car MAX-DOAS experiment and corresponding meteorological conditions over Beijing in January, September, and October, 2014.

Journey	Date	Time (BJT)	Wind speed (m/s)	Type of wind field*	Total cloud fraction	PBL Height (m)
1	2014/1/18	10:48-13:09	2	St	0	564
2	2014/1/19	13:31-15:40	1	O	7	167
3**	2014/1/21	13:15-15:32	3	S	0	163
4	2014/1/23	10:39-12:25	3	O	7	187
5	2014/1/23	13:07-15:12	2	O	7	163
6**	2014/1/24	10:42-12:03	2	N	8	39
7**	2014/1/24	13:03-15:09	3	N	8	39
8**	2014/1/26	10:21-12:13	5	S	5	341
9	2014/1/27	09:11-11:38	2	St	7	75
10**	2014/1/27	13:30-15:28	2	O	0	178
11**	2014/9/14	09:40-12:52	4	N	10	173
12**	2014/9/14	15:02-17:17	2	N	10	226
13	2014/9/17	09:07-11:42	2	St	7	173
14**	2014/9/19	09:09-11:50	2	S	3	178
15	2014/10/9	13:04-14:44	1	St	7	43
16**	2014/10/10	09:52-12:28	2	S	7	663
17**	2014/10/12	14:02-16:42	3	N	7	167
18**	2014/10/13	09:12-11:59	3	N	0	186
19	2014/10/13	13:11-16:27	3	O	0	130

*Four types of wind filed are South (S), North (N), Other (O), and Static (St).

740   **The data are preliminarily selected to estimate the NO_X emissions.

745

750

Table 2. Overview of the problems for the six circling journeys.

Date	Time (BJT)	Large wind variability *	Large lifetime correction*	Gap/route close to the centre*	Small difference between influx and outflux*	Multiple problems **
2014/1/26***	10:21-12:13	N	N	N	Y	N
2014/1/27***	13:30-15:28	Y	N	N	N	N
2014/9/14	09:40-12:52	Y	Y	Y	N	Y
2014/9/14***	15:02-17:17	N	Y	N	N	N
2014/10/12***	14:02-16:42	Y	Y	N	N	Y
2014/10/13***	09:12-11:59	Y	Y	N	N	Y

755   *Whether the condition meets the criteria of Shaiganfar et al. (2017) or not, Y and N denote Yes and No

respectively.

** Multiple problems mean whether more than two conditions can meet the criteria or not.

*** The data of five circling journeys are ultimately used to estimate the NOx emission.

760   Table 3. Error contributions (%) of multiple factors to the uncertainties in estimated E_{NOX} during five

circling journeys.

Factors	Jan. 26, AM	Jan. 27, PM	Sep. 14, PM	Oct. 12, PM	Oct. 13, AM
VCD_{geo}	10	10	10	10	10
Wind speed	27.02	26.83	7.97	33.10	3.68
Wind direction	10.97	16.50	20.54	33.78	38.37
NOx/NO_2 ratio	12.21	13.46	7.82	29.33	29.48
Lifetime	3.63	7.67	48.60	15.22	19.02

765

770
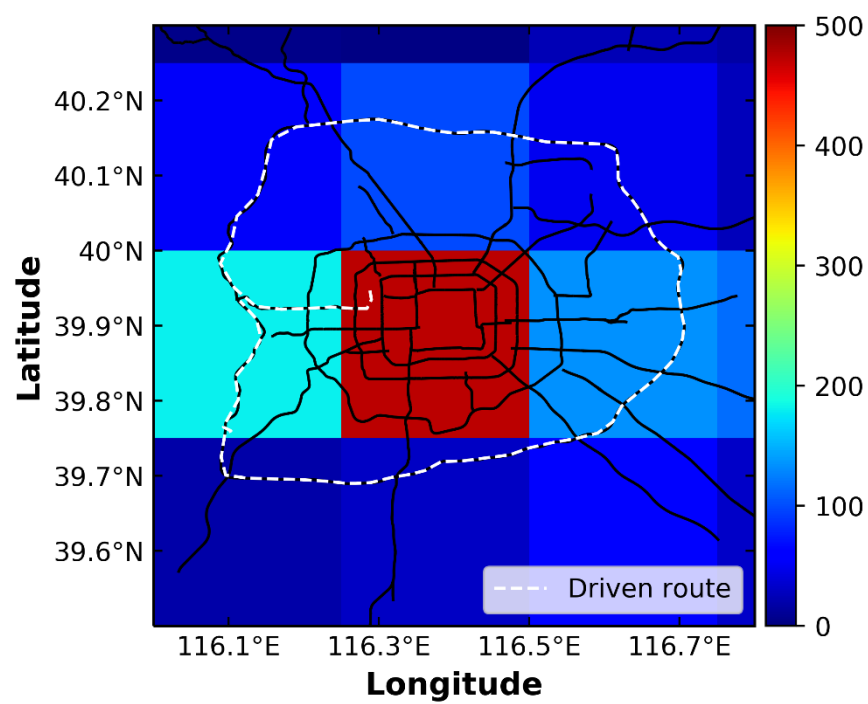
Fig. 1 Driving routes (white dash line) of the Car MAX-DOAS experiment on the 6th Ring Rd of Beijing
and distribution of yearly averaged NO_X emission rate (mole km^{-2} h^{-1}) from the MEIC for the year 2012.

775

780

785

790

795

800
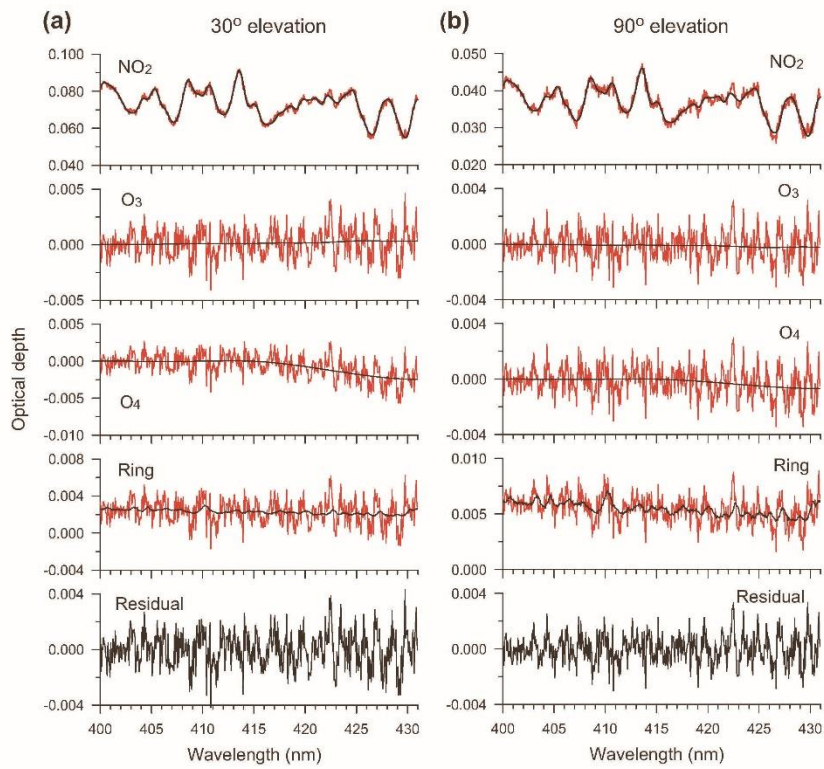
Fig. 2 Examples of the NO$_2$ retrieval from two successive spectra measured (**a**) at a 30° elevation angle (with NO$_2$ differential slant column density (DSCD) of 1.23×10^{17} molecules cm^{-2}) and (**b**) at a 90°

805   elevation angle (with NO$_2$ DSCD of 6.22×10^{16} molecules cm^{-2}) on January 18, 2014, at around 11:40 BJT.

810

815

820
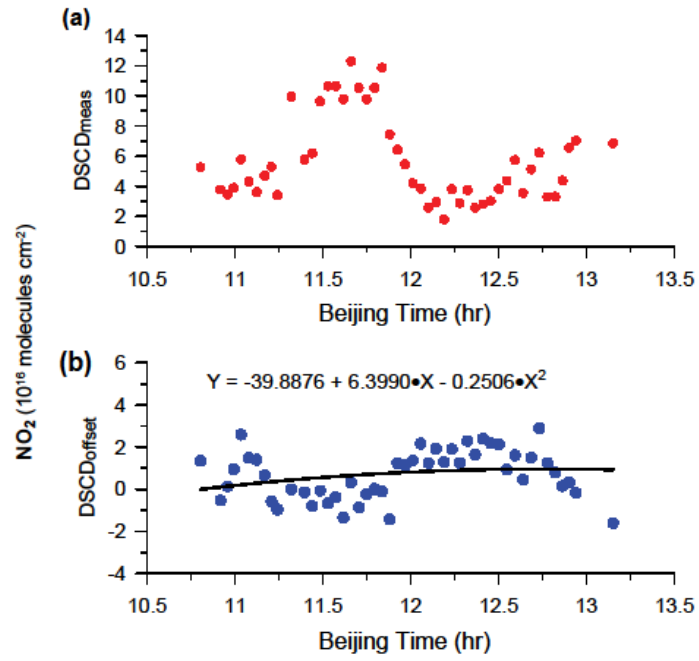
Fig. 3 Time series of the NO_2 (**a**) $DSCD_{means}$ (red dots) and (**b**) $DSCD_{offset}$ (black dots) (units of 10^{16} molecules cm^{-2}) for the 30° elevation angle of each sequence on January 18, 2014. The black curve

825   represents a second-order polynomial fit from individual $DSCD_{offset}$ data points.

830
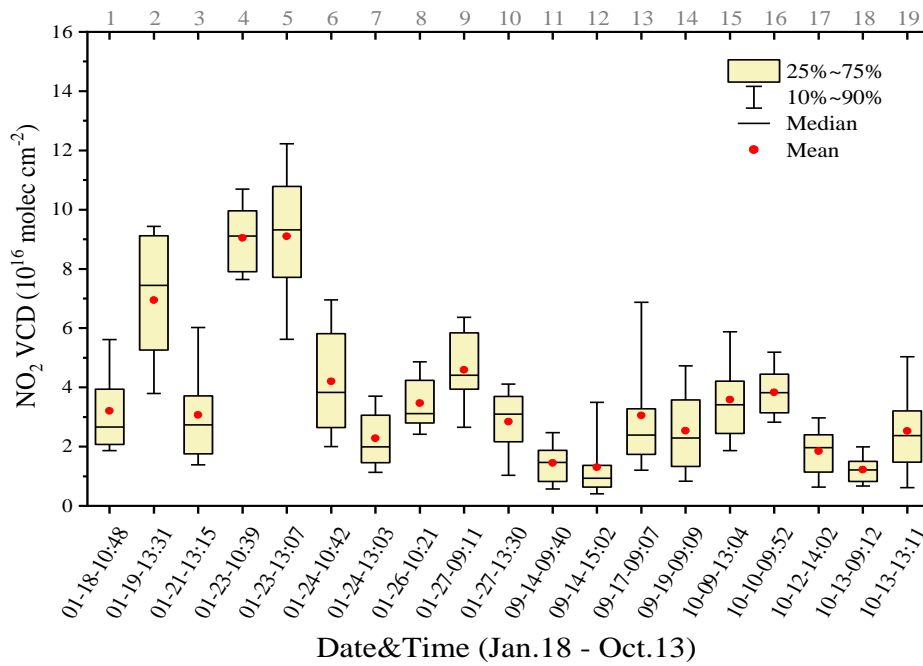
Fig. 4 Time series of the tropospheric NO_2 vertical column density (VCD) for 19 circling journeys on the Sixth Ring Road of Beijing in January, September, and October, 2014. Lower (upper) error bars and yellow boxes are the 10th (90th) and 25th (75th) percentiles of the data of each journey, respectively. Hyphens inside the boxes are the medians, and red circles are the mean values. The numbers of each journey are labeled at the top axis. See Table 1 for detailed information about each journey.
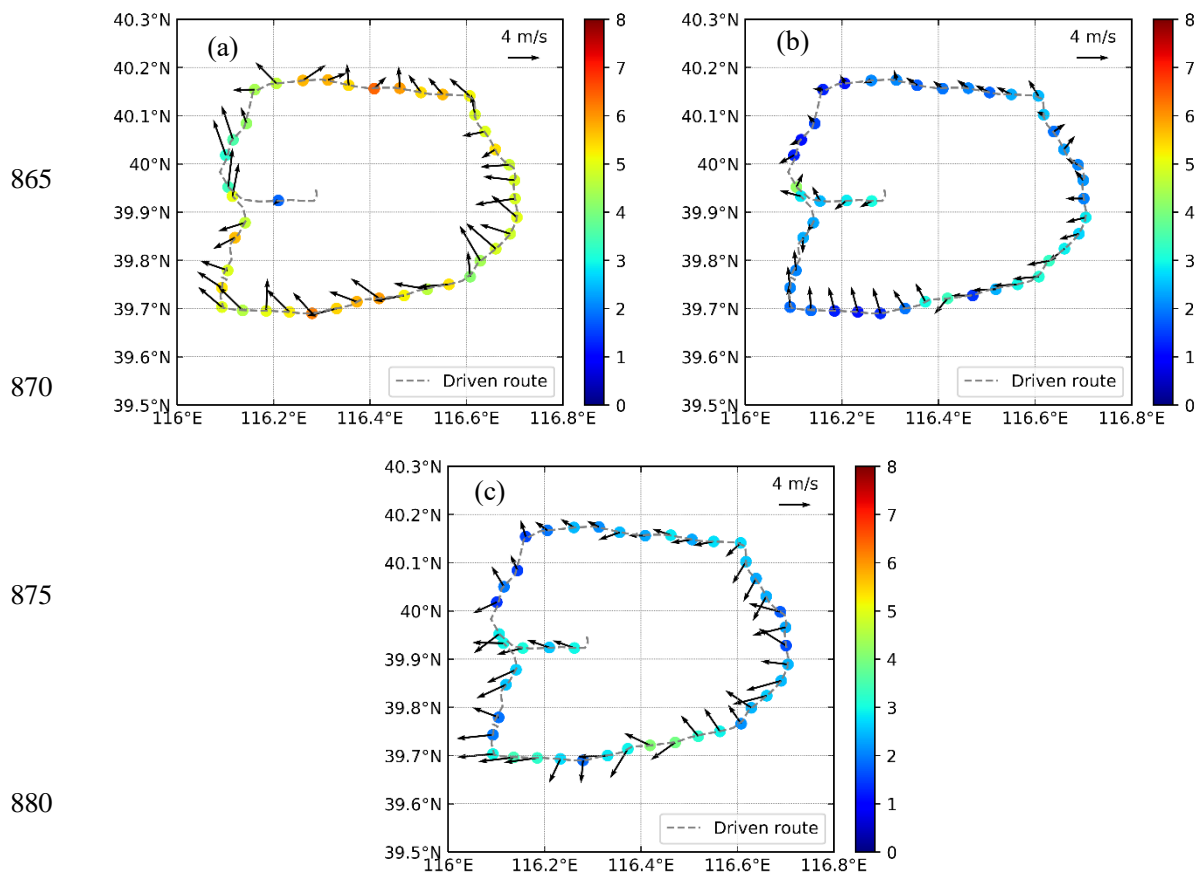
Fig. 5 Distributions of monthly averaged NO$_2$ VCD (10^{16} molecules cm^{-2}) on the 6th Ring Rd of Beijing in **(a)** January, **(b)** September, and **(c)** October, 2014.

905

910

915
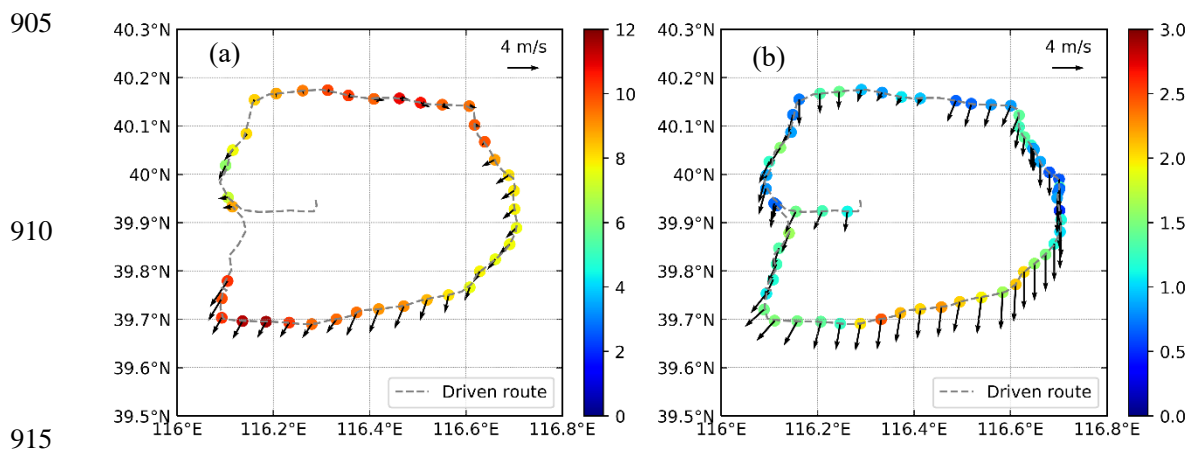
Fig. 6 Distributions of the maximum and minimum NO$_2$ VCD (10^{16} molecules cm^{-2}) on the 6th Ring

Rd of Beijing on the morning of **(a)** January 23 and **(b)** October 13, 2014.

920

925

930

935

940
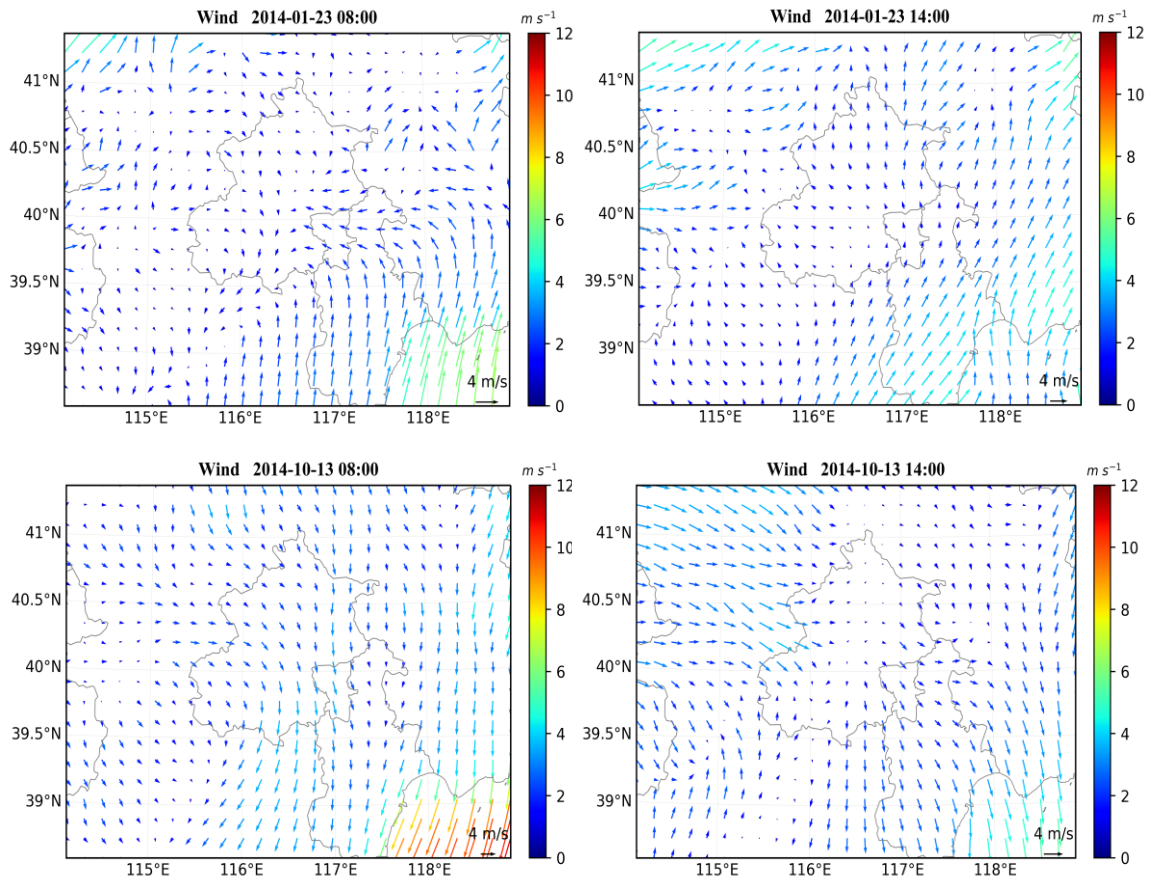
945 **Fig. 7** Wind fields in Beijing and the surrounding area from ECWRF at 08:00 (left column) and 14:00
(right column) BJT on January 23 and October 13, 2014.

950

955
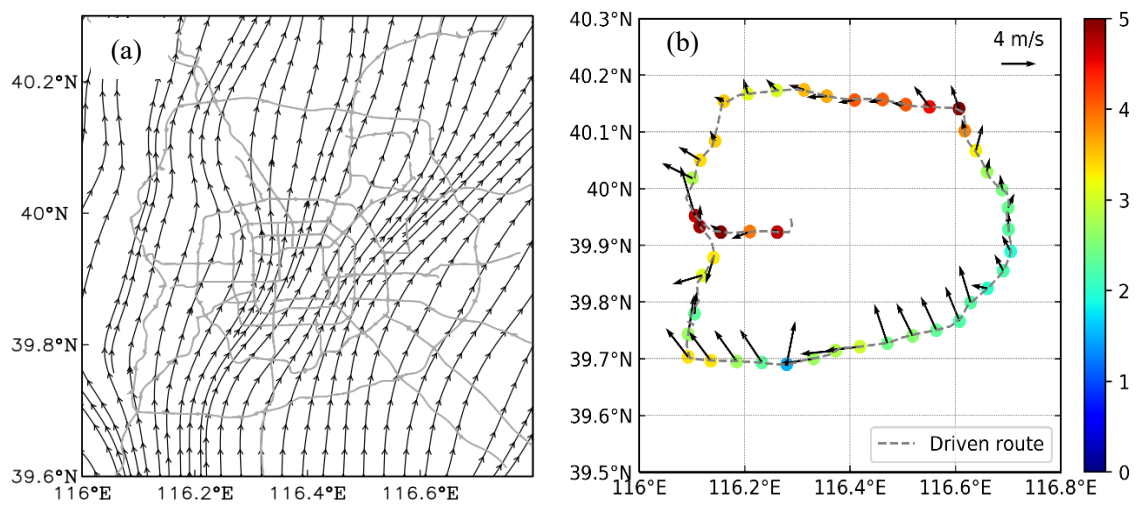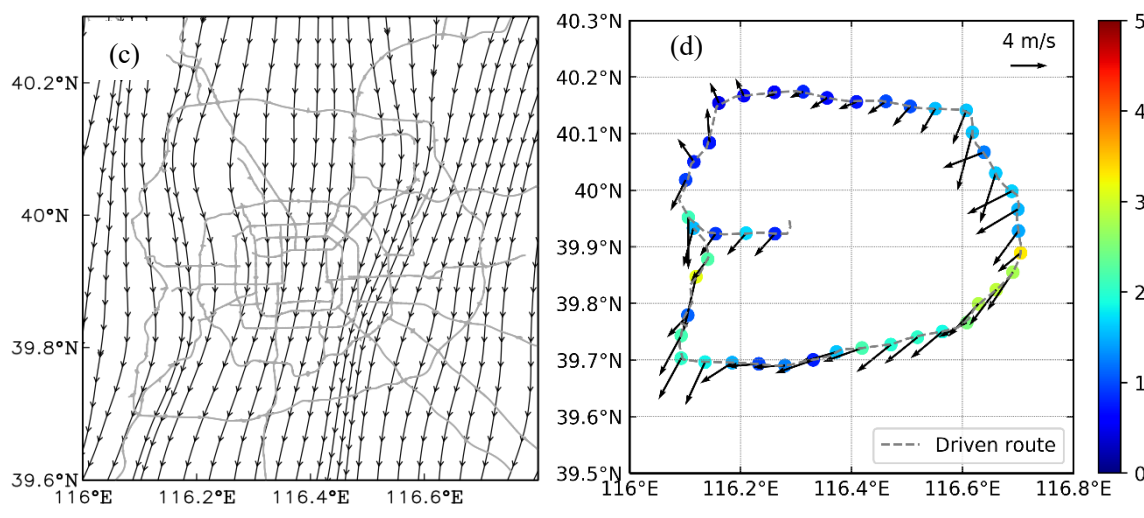
960

Fig. 8 Average wind stream and NO$_2$ VCD (10^{16} molecules cm^{-2}) distributions under the two different types of wind field over Beijing: **(a)** south wind, **(b)** NO$_2$ VCD under south wind, **(c)** north wind, and **(d)** NO$_2$ VCD under north wind.
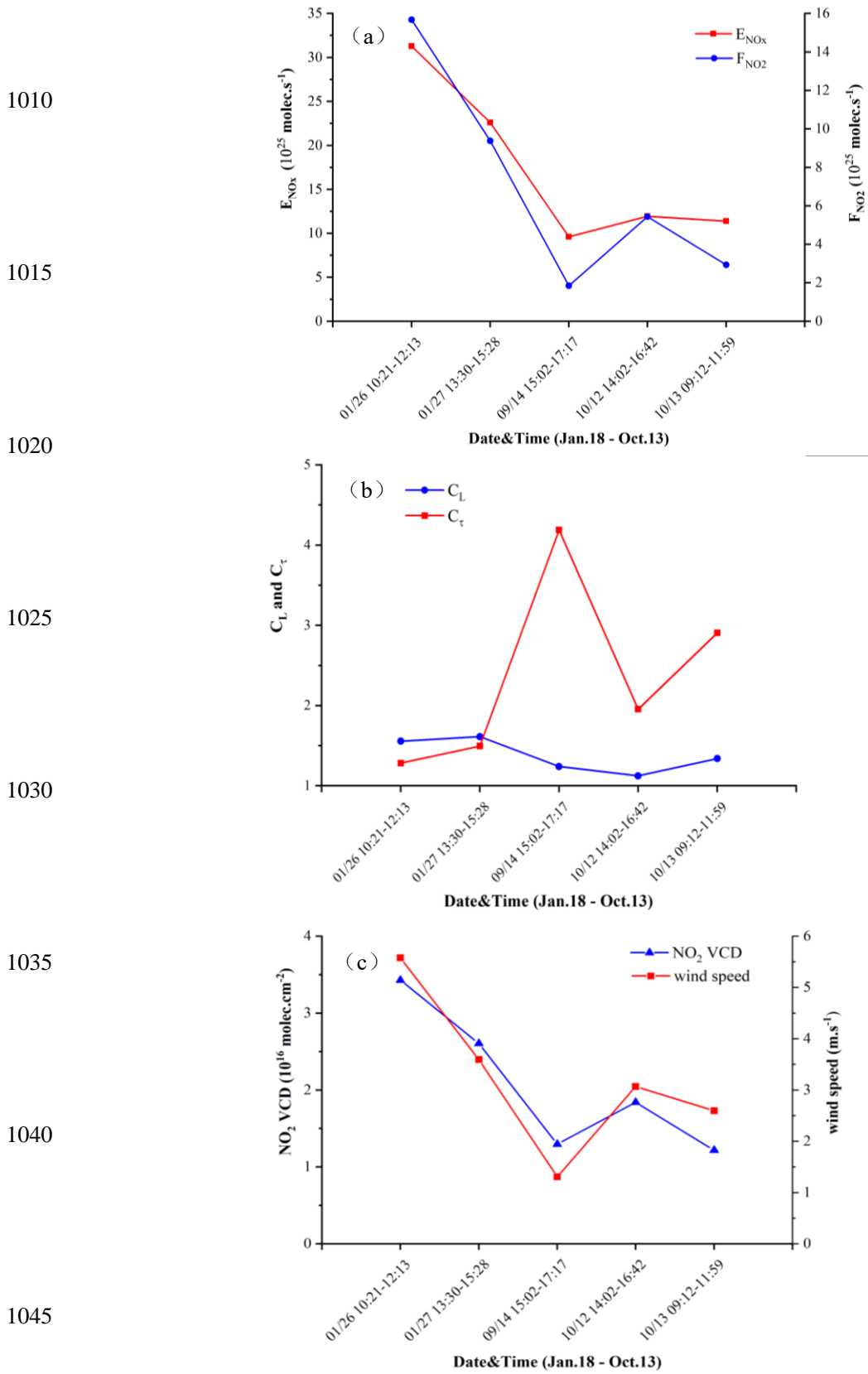
Fig. 9 Journey-to-journey variations in **(a)** F_{NO_2} and E_{NO_x}, **(b)** c_τ and c_L, **(c)** NO$_2$ VCD and mean wind

speed for five circling journeys on the 6th Ring Rd of Beijing in January, September, and October, 2014.
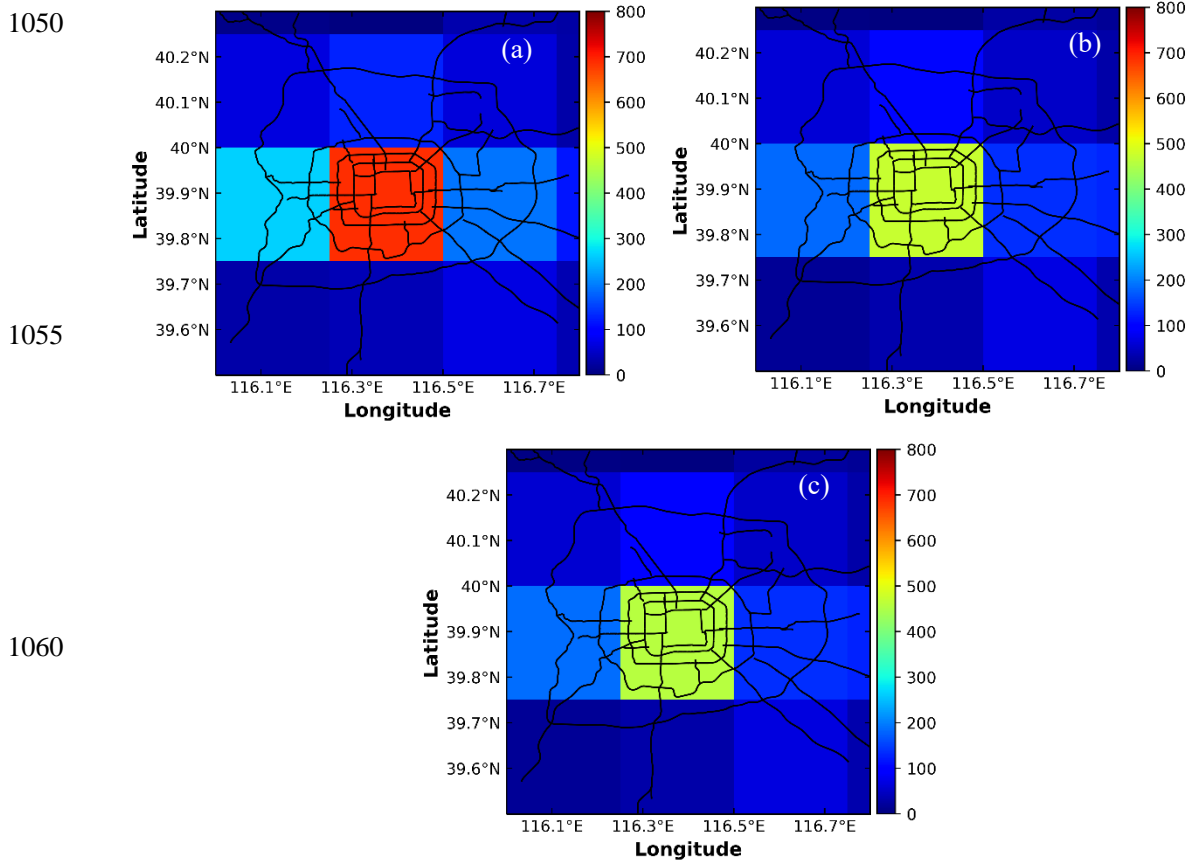
1050

1055

1060

Fig. 10 Spatial distributions of monthly averaged NO$_X$ emissions rate (mole km^{-2} h^{-1}) over Beijing based

1065 on the MEIC inventory in **(a)** January, **(b)** September, and **(c)** October in 2012.

1070

1075

1080
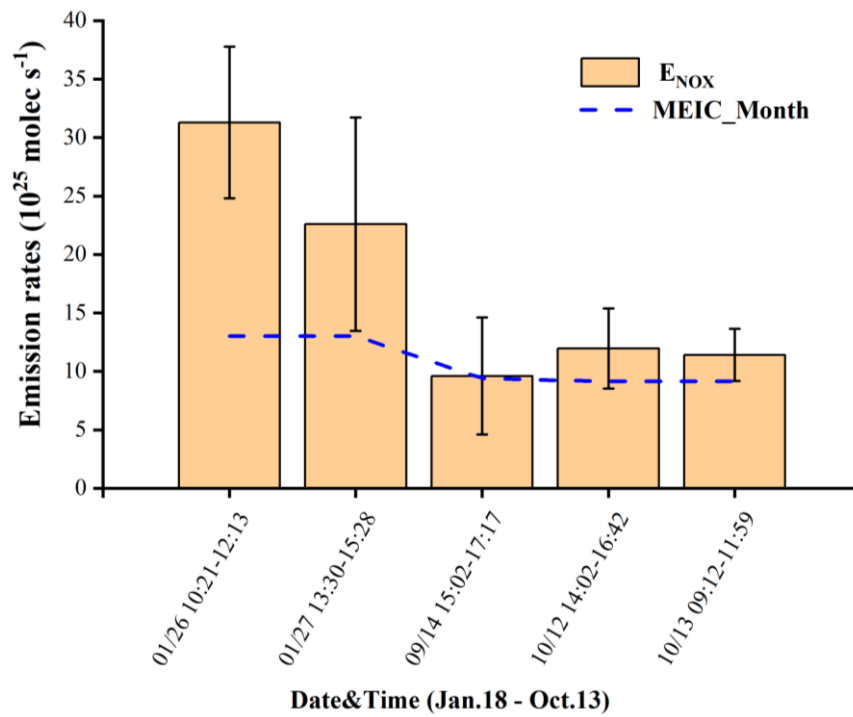
Fig. 11 Journey-to-journey variations in estimated E_{NO_x} and corresponding monthly emissions rate from the MEIC inventory (MEIC_Month) within the 6th Ring Rd of Beijing in January, September, and October 2014. Error bars represent the uncertainties in estimated E_{NO_x}